Search for Gamma-Ray Bursts with the ARGO-YBJ Detector in Shower Mode

B. Bartoli[1,2], P. Bernardini[3,4], X. J. Bi[5], Z. Cao[5], S. Catalanotti[1,2], S. Z. Chen[5], T. L. Chen[6], S. W. Cui[7], B. Z. Dai[8], A. D'Amone[3,4], Danzengluobu[6], I. De Mitri[3,4], B. D'Ettorre Piazzoli[1,9], T. Di Girolamo[1,2], G. Di Sciascio[9], C. F. Feng[10], Zhaoyang Feng[5], Zhenyong Feng[11], W. Gao[5], Q. B. Gou[5], Y. Q. Guo[5], H. H. He[5], Haibing Hu[6], Hongbo Hu[5], M. Iacovacci[1,2], R. Iuppa[12,13], H. Y. Jia[11], Labaciren[6], H. J. Li[6], C. Liu[5], J. Liu[8], M. Y. Liu[6], H. Lu[5], L. L. Ma[5], X. H. Ma[5], G. Mancarella[3,4], S. M. Mari[14,15], G. Marsella[3,4], S. Mastroianni[2], P. Montini[16], C. C. Ning[6], L. Perrone[3,4], P. Pistilli[14,15], P. Salvini[17], R. Santonico[9,18], P. R. Shen[5], X. D. Sheng[5], F. Shi[5], A. Surdo[4], Y. H. Tan[5], P. Vallania[19,20], S. Vernetto[19,20], C. Vigorito[20,21], H. Wang[5], C. Y. Wu[5], H. R. Wu[5], L. Xue[10], Q. Y. Yang[8], X. C. Yang[8], Z. G. Yao[5], A. F. Yuan[6], M. Zha[5], H. M. Zhang[5], L. Zhang[8], X. Y. Zhang[10], Y. Zhang[5], J. Zhao[5], Zhaxiciren[6], Zhaxisangzhu[6], X. X. Zhou[11], F. R. Zhu[11], and Q. Q. Zhu[5]

(The ARGO-YBJ Collaboration)

[1] Dipartimento di Fisica dell'Universitá di Napoli "Federico II," Complesso Universitario di Monte Sant'Angelo, via Cinthia, I-80126 Napoli, Italy
[2] Istituto Nazionale di Fisica Nucleare, Sezione di Napoli, Complesso Universitario di Monte Sant'Angelo, via Cinthia, I-80126 Napoli, Italy
[3] Dipartimento Matematica e Fisica "Ennio De Giorgi," Universitá del Salento, via per Arnesano, I-73100 Lecce, Italy
[4] Istituto Nazionale di Fisica Nucleare, Sezione di Lecce, via per Arnesano, I-73100 Lecce, Italy
[5] Key Laboratory of Particle Astrophysics, Institute of High Energy Physics, Chinese Academy of Sciences, P.O. Box 918, 100049 Beijing, China; chensz@ihep.ac.cn
[6] Tibet University, 850000 Lhasa, Xizang, China
[7] Hebei Normal University, 050024 Shijiazhuang Hebei, China
[8] Yunnan University, 2 North Cuihu Road, 650091 Kunming, Yunnan, China
[9] Istituto Nazionale di Fisica Nucleare, Sezione di Roma Tor Vergata, via della Ricerca Scientifica 1, I-00133 Roma, Italy
[10] Shandong University, 250100 Jinan, Shandong, China
[11] Southwest Jiaotong University, 610031 Chengdu, Sichuan, China; zhouxx@swjtu.edu.cn
[12] Dipartimento di Fisica dell'Universitá di Trento, via Sommarive 14, I-38123 Povo, Italy
[13] Trento Institute for Fundamental Physics and Applications, via Sommarive 14, I-38123 Povo, Italy
[14] Dipartimento di Fisica dell'Universitá "Roma Tre," via della Vasca Navale 84, I-00146 Roma, Italy
[15] Istituto Nazionale di Fisica Nucleare, Sezione di Roma Tre, via della Vasca Navale 84, I-00146 Roma, Italy
[16] Dipartimento di Fisica dell'Universitá di Roma "La Sapienza" and INFN—Sezione di Roma, piazzale Aldo Moro 2, I-00185 Roma, Italy
[17] Istituto Nazionale di Fisica Nucleare, Sezione di Pavia, via Bassi 6, I-27100 Pavia, Italy
[18] Dipartimento di Fisica dell'Universit'á di Roma "Tor Vergata," via della Ricerca Scientifica 1, I-00133 Roma, Italy
[19] Osservatorio Astrofisico di Torino dell'Istituto Nazionale di Astrofisica, via P. Giuria 1, I-10125 Torino, Italy
[20] Istituto Nazionale di Fisica Nucleare, Sezione di Torino, via P. Giuria 1, I-10125 Torino, Italy
[21] Dipartimento di Fisica dell'Universitá di Torino, via P. Giuria 1, I-10125 Torino, Italy

Abstract

The ARGO-YBJ detector, located at the Yangbajing Cosmic Ray Laboratory (4300 m a. s. l., Tibet, China), was a "full coverage" (central carpet with an active area of ∼93%) air shower array dedicated to gamma-ray astronomy and cosmic-ray studies. The wide field of view (∼2 sr) and high duty cycle (>86%), made ARGO-YBJ suitable to search for short and unexpected gamma-ray emissions like gamma-ray bursts (GRBs). Between 2007 November 6 and 2013 February 7, 156 satellite-triggered GRBs (24 of them with known redshift) occurred within the ARGO-YBJ field of view (zenith angle $\theta \leqslant 45°$). A search for possible emission associated with these GRBs has been made in the two energy ranges 10–100 GeV and 10–1000 GeV. No significant excess has been found in time coincidence with the satellite detections nor in a set of different time windows inside the interval of one hour after the bursts. Taking into account the EBL absorption, upper limits to the energy fluence at a 99% confidence level have been evaluated, with values ranging from $\sim 10^{-5}$ erg cm^{-2} to $\sim 10^{-1}$ erg cm^{-2}. The *Fermi*-GBM burst GRB 090902B, with a high-energy photon of 33.4 GeV detected by *Fermi*-LAT, is discussed in detail.

Key words: gamma-ray burst: general

1. Introduction

Gamma-ray bursts (GRBs) are the brightest explosions of gamma-rays observed so far, occurring at unpredictable times and random directions in the sky. After almost 50 years since their discovery (Klebesadel et al. 1973), GRBs are still some of the most enigmatic astrophysical phenomena. Up to now, over 6000 GRBs with gamma-rays of energies from keV to MeV have been observed by dedicated satellites as CGRO-BATSE (Kouveliotou et al. 1993), Beppo SAX (Van et al. 1997), *HETE*-2 (Berger et al. 2003), *Swift* (Cusumano et al. 2006), and *Fermi*-GBM (Narayana Bhat et al. 2016). The results of BATSE (on board the CGRO) showed that the arrival

directions of GRBs are highly isotropic, favoring a cosmological origin (Meegan et al. 1992). Thanks to the launch of Beppo SAX, which provided a precise localization of several GRBs, the first redshifts could be measured, proving that GRB sources are cosmological objects (Metzger et al. 1997). Now more than 470 redshifts have been measured, ranging from $z = 0.0085$ for GRB980425[22] to the value of $z = 8.1$ for GRB090423 (Salvaterra et al. 2009). These data confirm that most GRBs indeed originate at cosmological distances and hence are likely among the most energetic phenomena that ever occurred since the Big Bang.

---

[22] http://www.mpe.mpg.de/~jcg/grb980425.html

The time duration of GRBs usually ranges from a few seconds to tens of seconds, but occasionally can be as long as a few tens of minutes or as short as a few milliseconds. According to the T_{90} parameter, defined as the time interval in which 90% (from 5% to 95%) of the GRB photons is released, GRBs are usually classified into long ($T_{90} > 2$ s) and short ($T_{90} \leqslant 2$ s) bursts (Kouveliotou et al. 1993). Short GRBs are mostly associated with mergers of compact objects while long GRBs are related to collapsars (Rosswog et al. 2003; Fox et al. 2005; Bloom et al. 2006; Campana et al. 2006; Larsson et al. 2015; Zhang 2016).

The GRB photons detected by satellite instruments are mostly in the keV–MeV energy range. Thanks to EGRET (on board the CGRO) and LAT (on board *Fermi*), both designed to detect photons in the MeV–GeV energy range, 74 GRBs (up to the time of writing, 2017 March 20) have been observed to contain photons of energy above 1 GeV, and for 20 of them, photons of energy above 10 GeV have been detected (Hurley et al. 1994; *Fermi*-LAT GRBs website[23]). In particular, *Fermi*-LAT announced the detection of a 95 GeV photon in coincidence with GRB 130427A (Ackermann et al. 2014), the highest energy observed so far from a burst. From these observations, we know that at least a fraction of GRBs has a high-energy tail, reaching 1–10 GeV or even more. At the same time, some theoretical models also predict the emission of high-energy photons from GRBs (Ma et al. 2003; Beloborodov et al. 2014; Hascoët et al. 2015).

Though much progress has been achieved from satellite-based experiments and theoretical efforts, many basic questions still remain unresolved (Ackermann et al. 2014). Which are the energy source and the acceleration mechanism of GRBs? Is there a GRB originating in our Galaxy? In order to understand the whole picture of the process, it is important to improve the sample of GRBs with high-energy emission and to measure the multi-wavelength energy spectrum. Furthermore, since the flux of high-energy photons should be strongly attenuated by the interaction with the extragalactic background light (EBL), the detection of photons with energy above 10 GeV from high-redshift sources could be of extreme importance in constraining the EBL theoretical models.

Due to the limited size of the space detectors and the rapid fall of GRB energy spectra, satellite-based experiments hardly cover the energy region $E > 10$–100 GeV. Ground-based experiments, including imaging atmospheric Cherenkov telescopes (IACTs) and extensive air shower (EAS) arrays, can easily reach much larger effective areas, and can be used for the detection of the GRBs high-energy component. Searches for GeV–PeV emission from GRBs have been done by many ground-based experiments, such as MAGIC (Albert et al. 2006; Aleksić et al. 2014), HESS (Abramowski et al. 2014), VERITAS (Acciari et al. 2011), Milagrito (Atkins et al. 2000, 2005; Abdo et al. 2007), GRAND (Poirier et al. 2003), HEGRA (Padilla et al. 1998), HAWC (Abeysekara et al. 2015), EAS-TOP (Aglietta et al. 1996), INCA (Castellina et al. 2001), Tibet ASγ (Amenomori et al. 1996; Ding et al. 1997; Zhou et al. 2009), and IceCube (Aartsen et al. 2016). However, no significant events have been observed so far, though some positive indications have been reported. The science prospects for GRBs with CTA have been provided by Inoue et al. (2013). The EAS array

LHAASO is currently under construction in Sichuan, China, at 4410 m a. s. l. and will begin to take data with a partial array in 2018. The prospects for GRB detection with LHAASO have been discussed by Chen et al. (2015).

Besides a wide field of view and a high duty cycle (fundamental detector properties for the observation of unpredictable and short duration events such as GRBs), ARGO-YBJ has two additional key features—the high altitude and the full coverage—making possible the detection of very small showers generated by gamma-rays of energy well below 1 TeV. This capability is essential for the GRB detection, since photons of higher energy originated at cosmological distances are mostly absorbed in the extragalactic space due to pair production with the UV, optical, and infrared photons of EBL.

The GRB search by ARGO-YBJ can be done with two different techniques: scaler mode (Vernetto 2000) and shower mode. In scaler mode, the data are the single particle counting rate of the detector. A burst candidate would appear as an excess of counts in coincidence with a satellite GRB with no information about the GRB direction. In shower mode, the events are reconstructed and their arrival direction and energy are measured with an offline process, and a burst candidate would appear as an excess of showers with the arrival direction consistent with that of the satellite GRB. The selection of showers according to their direction significantly decreases the background with respect to the scaler mode. On the other hand, the requirement of a minimum number of particles to trigger the detector increases the primary energy threshold.

The ARGO-YBJ results of a search in scaler mode in coincidence with satellite GRBs have been reported in Aielli et al. (2009a) and in Bartoli et al. (2014a) in the energy range of 1–100 GeV. In shower mode, the study of the sensitivity to detect GRBs is given by Zhou et al. (2007, 2016), while the results of a first search for GRBs using the data recorded before 2009 January are reported in Aielli et al. (2009b). The results in shower mode concerning the whole sample of data recorded during the ARGO-YBJ lifetime, from 2007 November 6 to 2013 February 7, will be presented and discussed in this paper.

2. The ARGO-YBJ Experiment

The ARGO-YBJ experiment, located at the Yangbajing Cosmic Ray Laboratory in Tibet, China, at an altitude of 4300 m a. s. l., was mainly devoted to gamma-ray astronomy (Bartoli et al. 2013, 2014b, 2015a) and cosmic-ray physics (Bartoli et al. 2015b, 2015c). The detector is composed of a single layer of resistive plate chambers (RPCs), operated in streamer mode, with a modular configuration. The basic module is a cluster ($5.7 \times 7.6\,\mathrm{m}^2$), composed of 12 RPCs ($1.23 \times 2.85\,\mathrm{m}^2$ each). Each RPC is read out by 10 pads ($55.6 \times 61.8\,\mathrm{cm}^2$ each), representing the spacetime pixels of the detector. The clusters are disposed in a central full-coverage carpet (130 clusters on an area of $74 \times 78\,\mathrm{m}^2$ with an active area of $\sim$93%). In order to improve the performance of the experiment in determining the shower core position, the central carpet is surrounded by 23 additional clusters ("guard ring"). The total area of the array is $110 \times 100\,\mathrm{m}^2$. More details of the detector can be found in Aielli et al. (2006). The installation of the whole detector was completed in the spring of 2007, and the data taking started in 2007 November with a trigger rate of $\sim$3.5 kHz. In 2013 February, the detector was definitively switched off.

---

[23] http://fermi.gsfc.nasa.gov/ssc/observations/types/grbs/lat_grbs
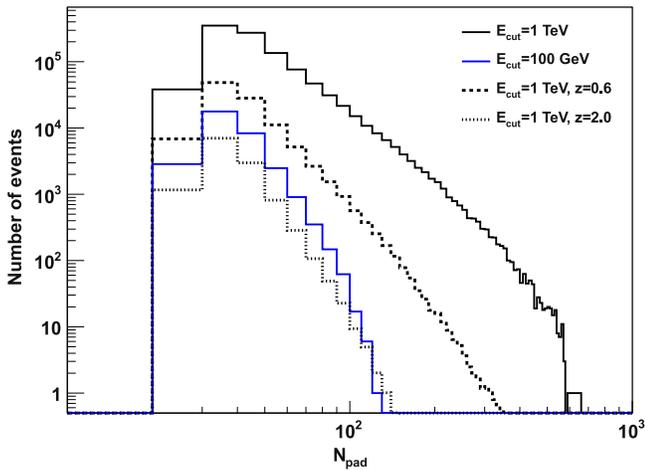
Figure 1. N_{pad} distribution for gamma-rays in the energy range of 10–100 GeV and 10–1000 GeV.

Table 1
N_{pad} Ranges and Corresponding Angular Window Radii for Gamma Rays in
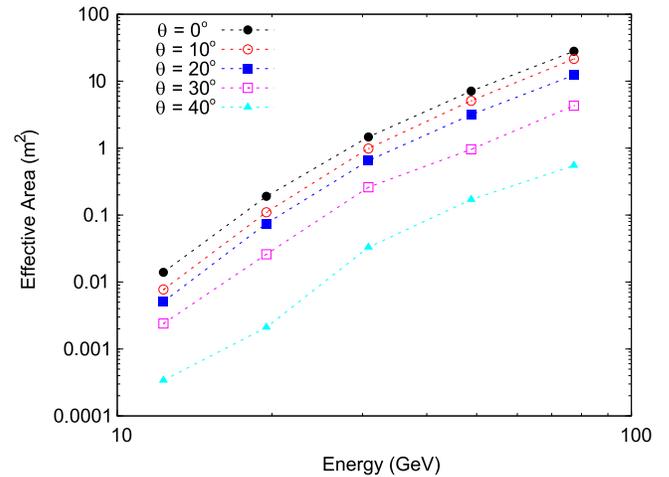Two Different Energy Ranges

Energy (GeV)	N_{pad}	Ψ_{70} (°)
10–100	20–60	3.8
10–1000	20–500	2.6

The ARGO-YBJ detector was connected to two independent data acquisition systems, corresponding to the shower and scaler operation modes. In the scaler mode, the total counts of each cluster are recorded every 0.5 s. In the shower mode, the detector is triggered when at least 20 pads in the central carpet are fired within a time of 420 ns. The information on the arrival time and location of each hit are recorded to reconstruct the shower front shape and the arrival direction. These data are used for gamma astronomy studies and to the search of GRBs in shower mode.

3. Data Selection and Analysis

From 2007 November 6 to 2013 February 7, 188 GRBs occurred in the ARGO-YBJ field of view (zenith angle $\theta \leqslant 45°$). 99 of them were detected by *Fermi* (selected from the *Fermi*-GBM Burst Catalog website[24]) and 89 were detected by *Swift* and other detectors (selected from *Swift* and GCN web sites[25]). The present analysis is carried out on 156 of them, since the remaining 32 occurred when the detector was not operating, or the localization by *Fermi* was too poor (i.e., error boxes larger than 10°).

As GRB photons of energy above $\sim$1 TeV (or even below, for very large distances) are likely to be absorbed by the EBL, we assume a GRB power-law spectrum with a sharp cutoff E_{cut} at two different maximum energies: 100 GeV and 1 TeV. Since showers generated by photons of energy $E < 10$ GeV cannot trigger the ARGO-YBJ detector, we limit our search to the two energy ranges 10–100 GeV and 10–1000 GeV. The selection of events with these primary energies is done by selecting the showers according to the number of fired pads (N_{pad}). The

[24] http://heasarc.gsfc.nasa.gov/W3Browse/fermi/fermigtrig.html
[25] http://swift.gsfc.nasa.gov/archive/grb_table; http://gcn.gsfc.nasa.gov/gcn3_archive.html

Figure 2. Effective area of ARGO-YBJ for events with $N_{pad} = 20$–60 and different zenith angles, as a function of the primary energy.

number of fired pads is related to the gamma-ray energy, but for a given energy the number of pads has a large distribution, mainly depending on the fluctuations of shower development and on the position of the shower core with respect to the center of the detector. In this analysis, the primary energy is not reconstructed. To evaluate the N_{pad} intervals optimized for the two energy ranges considered, we use Monte Carlo simulations: the CORSIKA7.3700 code to describe the development of extensive air showers in the atmosphere, and a code based on GEANT4 (Agostinelli et al. 2003) to simulate the detector response. Figure 1 shows the N_{pad} distributions assuming a gamma-ray power-law spectrum with index -2 and cutoff at 100 GeV and 1 TeV, respectively, for events with zenith angles smaller than 45°. We found that the N_{pad} intervals that optimize the detection of gamma-rays with the assumed spectra (i.e., that maximizes the signal-to-noise ratio) are $N_{pad} = 20$–60 for $E = 10$–100 GeV and $N_{pad} = 20$–500 for $E = 10$–1000 GeV (Table 1). In the same figure, the N_{pad} distributions produced by spectra with $E_{cut} = 1$ TeV affected by the EBL absorption are also shown, for redshifts $z = 0.6$ and 2. To describe the absorption effects, we used the optical depths evaluated by Gilmore et al. (2012). For redshift $z = 2$, the N_{pad} distribution is similar to the one with $E_{cut} = 100$ GeV, since gamma-rays of energy above 100 GeV are strongly absorbed by EBL. From the figure, it is clear that the $N_{pad} = 20$–60 interval is suitable for the detection of a typical "long GRB" with redshift around 2, while the $N_{pad} = 20$–500 interval is suitable for nearby GRBs with the extended spectrum.

The detector effective area A_{eff} for events with $N_{pad} = 20$–60 and $N_{pad} = 20$–500 has been calculated for gamma-ray energy ranging from 10 to 1000 GeV using the expression:

$$A_{eff}(E, \theta) = \frac{n_s}{N} \cdot A_s \cdot \cos\theta, \qquad (1)$$

where n_s is the number of successfully reconstructed shower events in a given N_{pad} range, N is the total number of events generated by CORSIKA, and A_s is the sampling area (200×200 m^2). Figures 2 and 3 show the effective area as a function of the primary energy in the two N_{pad} ranges, for different zenith angles. The effective area for vertical showers with $N_{pad} = 20$–60 ranges from $\sim$0.01 m^2 at 10 GeV to $\sim$50 m^2 at 100 GeV, while the effective area reaches
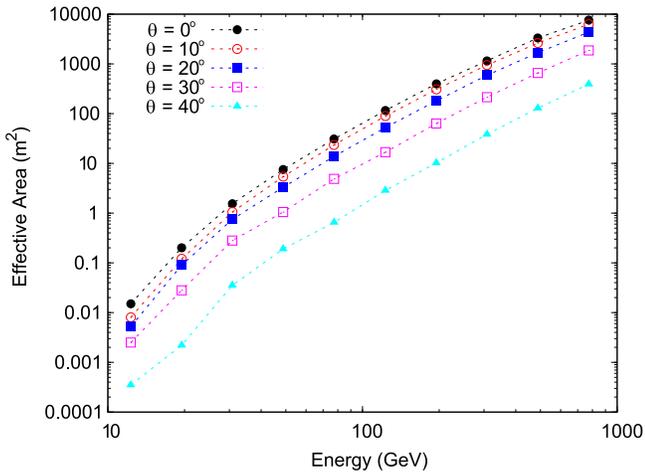
Figure 3. Effective area of ARGO-YBJ for events with $N_{pad} = 20$–500 and different zenith angles, as a function of the primary energy.
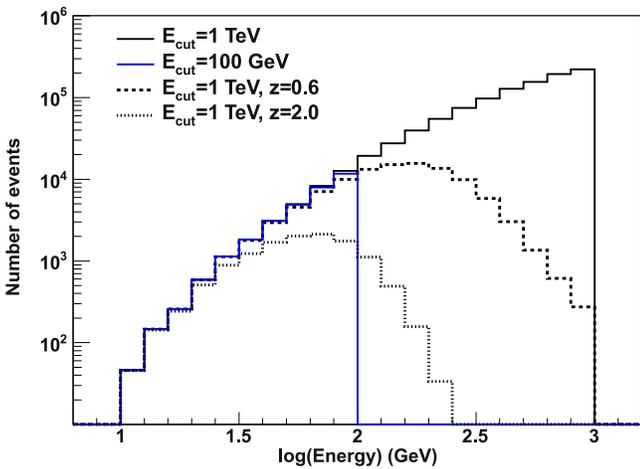
Figure 4. Gamma-ray energy distribution corresponding to events with $N_{pad} = 20$–60 for $E_{cut} = 100$ GeV, and $N_{pad} = 20$–500 for $E_{cut} = 1$ TeV.

$\sim$10,000 m^2 at 1 TeV using the events with $N_{pad} = 20$–500. The effective areas significantly decrease at large zenith angles. At 100 GeV, the effective area for $\theta = 30°$ (40°) is about a factor of 6 (50) smaller than for vertical photons.

The effective area, folded with the gamma-ray spectrum, determines the energy distribution of the detected events. Figure 4 shows the energy distribution of events in the two N_{pad} intervals previously defined, obtained by simulating a gamma-ray spectrum with different cutoff energies. The spectral index is assumed equal to -2, and the gamma-ray zenith angle smaller than 45°. The corresponding median energies of the distributions are 70 GeV and 540 GeV for $E_{cut} = 100$ GeV and 1 TeV, respectively. Adding the EBL absorption to the spectrum with $E_{cut} = 1$ TeV, the median energies decrease to 60 GeV and 150 GeV for $z = 2$ and $z = 0.6$, respectively.

In the ARGO-YBJ data, a GRB would appear to be an excess of showers with arrival directions concentrated in a small sky window, whose size is related to the angular resolution of the detector. In our analysis, the radius of the search window (defined as the "on-source window") is chosen to maximize the signal to background ratio. According to

simulations, the best opening angle radius Ψ_{70} is 3°.8 and 2°.6 for the two N_{pad} ranges adopted in the analysis, respectively, and contains 71.5% of the signal events.

Due to the different angular resolution to determine the arrival direction of GRBs by different satellite experiments, the position of our on-source window is defined by two approaches. For the 78 GRBs detected by *Swift* and other satellites excluding *Fermi* (we call them for simplicity "*Swift* GRBs" since the large majority of them has been detected by *Swift*), the position is determined with a precision much better than the angular resolution of ARGO-YBJ. In this case, the on-source window is centered at the position reported by the satellite. For 77 of 78 GRBs detected by *Fermi*-GBM (we call them "*Fermi* GRBs"), the uncertainty in the position is often greater than 1° (Connaughton et al. 2015). In this case, our on-source window is shifted inside the *Fermi* error box, by steps of $\Psi_{70}/2$ in right ascension and declination, to cover the whole region (defined by including statistical and systematic uncertainty with a 68% confidence level). GRB 090902B, even if detected by *Fermi*, has been analyzed as a "*Swift* GRB" because of the precise localization determined by *Swift*.

From the observations of satellite instruments (Hurley et al. 1994; Abdo et al. 2009) and some theoretical models (Dermer & Chiang 2000; Pe'er & Waxman 2004), we know that the acceleration mechanism for high-energy gamma-rays could be different from that at low energies, and consequently the burst start time and duration could be different from what was recorded in the keV–MeV energy range. The *Fermi*-LAT results and recent models all show that the high-energy emissions from GRBs are in the prompt phase or at delayed times (Hascoët et al. 2015). To take into account these possibilities, our search for GRB counterparts is performed in the hour following the GRB satellite trigger time. To investigate possible different durations of the high-energy emission, we use the T_{90} given by satellite measurements, and also the time windows $\Delta t = 0.5, 1, 3, 6, 12, 24, 48$, and 96 s, that are shifted by steps of 0.25, 0.5, 1, 2, 3, 6, 12, and 24 s, respectively, inside the interval of one hour after the GRB start time.

For each trial, defined by time duration, start time and on-source window position, we compare the number of detected events N_{on} with the number of the expected background events $\langle N_b \rangle$ due to cosmic rays, and we calculate, using the Poisson statistics, the chance probability P_b of having a number of events equal to or larger than N_{on}, and the corresponding statistical significance S in standard deviations (s.d.).

The number of the expected background events $\langle N_b \rangle$ is estimated using the "equi-zenith-angle" method (Zhou 2003), i.e., using the events with the same zenith angle but with different azimuth, detected during two hours around the GRB time. The choice of this time interval comes from the observation that the cosmic-ray detection rate (that can fluctuate up to a few percent on timescales of several hours due to atmospheric pressure and temperature variations) in two hours can be considered stable enough for our purposes. Note that due to the atmospheric absorption the background rate is strongly dependent on the zenith angle. As an example, Figure 5 shows the average background event rate $\langle N_b \rangle$ as a function of the zenith angle, measured during two hours around the time of GRB110705364, for the two angular windows of radius 3°.8 and 2°.6.
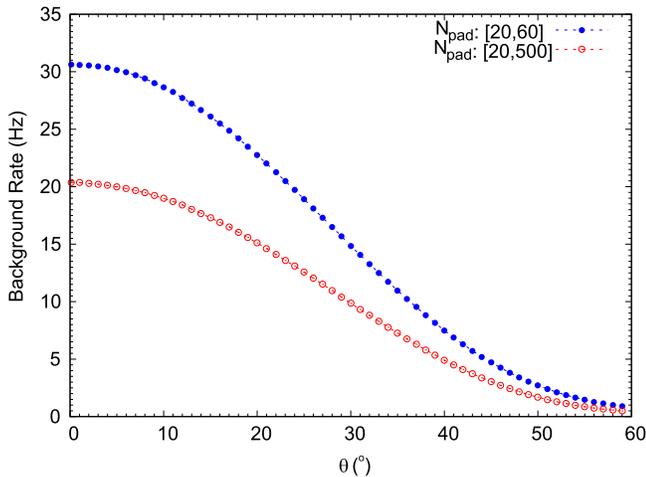
Figure 5. Background event rate as a function of the zenith angle, inside the angular windows used for the analysis in two N_{pad} ranges. The data have been recorded during two hours around the GRB110705364 trigger time.

4. Results

4.1. Analysis of Swift GRBs

The distribution of the chance probability P_b for all the events in coincidence with the 79 *Swift* GRBs is shown in Figure 6, while the corresponding significances S are given in Figure 7. These figures show the results of the analysis in the two N_{pad} ranges previously defined, merged together. The significance distribution is consistent with a Gauss function (solid black line in the figure), showing that the signals are consistent with background fluctuations. It is, however, interesting to report the details of the most significant excesses.

For the N_{pad} range of 20–60, the excess with the lowest probability is related to GRB080207, whose position (α_o, δ_o) determined by *Swift* is $(13^h50^m03^s.12, 07^o31'01'')$. It is delayed by 2502 s, and occurs at a zenith angle of $23°.5$. This excess consists of 746 showers in 24 s, while the expected number of background events is 617.96. The corresponding poissonian chance probability is 2.98×10^{-7}, with a significance of 5.0 s.d.. Taking into account the number of trials (2.05×10^6), the chance probability is 6.11×10^{-1} (-0.28 s.d.).

For the N_{pad} range of 20–500, the lowest probability excess refers to GRB081025, whose position (α_o, δ_o) determined by *Swift* is $(16^h21^m11^s.52, 60^o27'58'')$. It is delayed by 3186 s, and occurs at a zenith angle of $32°.8$. This excess consists of 28 air showers in 1 s, while the expected number of background events is 8.88. The chance probability is 1.53×10^{-7}, corresponding to 5.12 s.d.. After taking into account for the number of trials, the chance probability is 3.13×10^{-1} (0.49 s.d.).

4.2. Analysis of Fermi GRBs

The distribution of the chance probability P_b for all the events in coincidence with 77 *Fermi* GRBs is shown in Figure 8, while the corresponding significances S are given in Figure 9. Also in this case the distributions show no statistically significant excess for this sample.

For the N_{pad} range of 20–60, the lowest probability excess is related to GRB081122520, whose position (α_o, δ_o) determined by *Fermi* is $(22^h36^m24^s, 40^o00'00'')$ with an angular indetermination of $3°.8$. The excess is centered at $(\alpha, \delta) = (22^h51^m35^s.98, 40^o00'00'')$, at a zenith angle of $10°.0$. It is delayed by 1176 s and
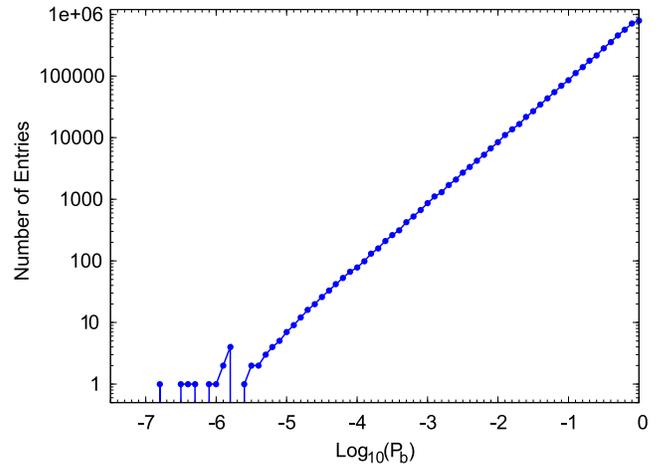
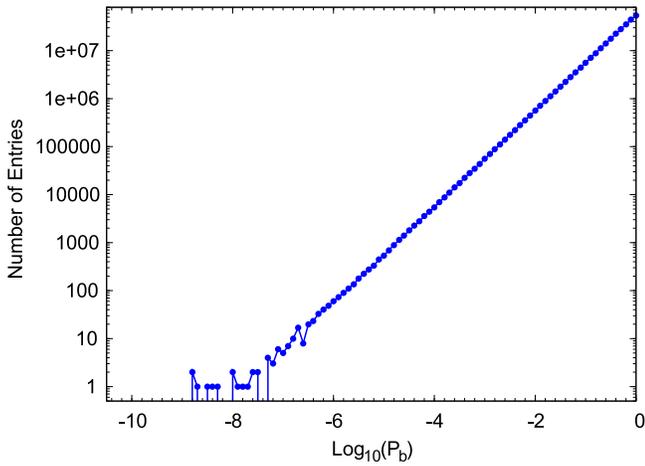**Figure 6.** Probability distribution of the 4.1×10^6 trials in coincidence with 79 *Swift* GRBs.
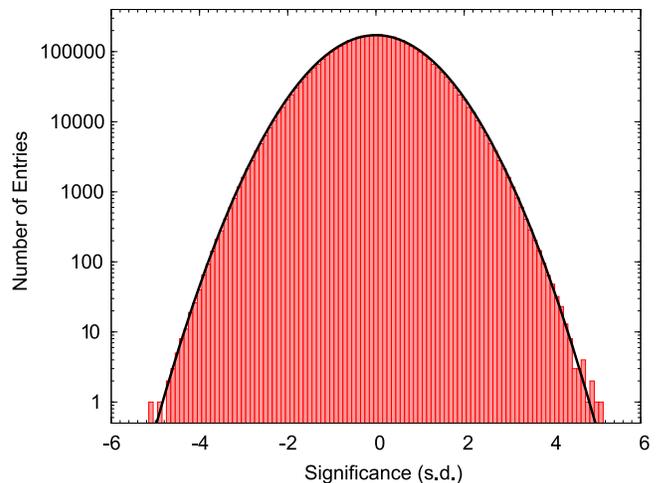
Figure 7. Significance distribution of the 4.1×10^6 trials in coincidence with 79 *Swift* GRBs. The solid black line is the normal Gaussian function.

consists of 855 air showers in 24 s, while the expected number of background events is 693.4. The chance probability is 1.57×10^{-9}, corresponding to a significance of 5.92 s.d.. Taking into account the number of trials (9.01×10^7), the chance probability becomes 1.41×10^{-1} (1.07 s.d.).

For the N_{pad} range of 20–500, the lowest probability excess is connected to GRB100210101, whose position (α_o, δ_o) determined by *Fermi* is $(16^h17^m31^s.2, 16^o04'48'')$ with an uncertainty of $7°.1$. The excess is centered at $(\alpha, \delta) = (16^h07^m07^s.18, 12^o10'48'')$, at a zenith angle of $32°.1$. It is delayed 881 s and consists of 64 air showers in 3 s, while the expected number of background events is 27.5. The chance probability is 1.38×10^{-9}, corresponding to a significance of 5.95 s.d.. After taking into account the number of trials (1.79×10^8), the chance probability is 2.47×10^{-1} (0.68 s.d.).

5. Upper Limits to the Energy Fluence in T90

Since no significant excess has been found in coincidence with 156 satellite-triggered GRBs, we calculate the upper limits to the energy fluence for the two energy ranges considered in the analysis. The fluence upper limits are evaluated during the prompt phase of the emission, i.e., in the time interval T_{90}. Figures 10 and 11 show the significance distributions of the

Figure 8. Probability distribution of the 2.69×10^8 trials in coincidence with 77 *Fermi* GRBs.
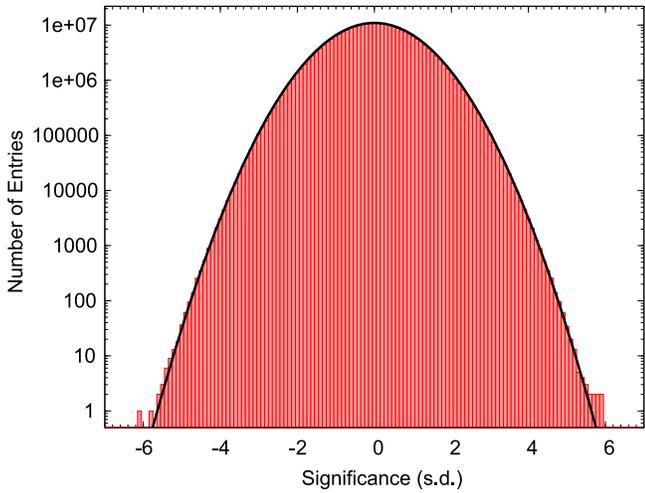
Figure 9. Significance distribution of 2.69×10^8 trials in coincidence with 77 *Fermi* GRBs. The solid black line is the normal Gaussian function.

Figure 10. Significance distribution of the events detected in coincidence with the prompt phase of 156 GRBs, for the N_{pad} range of 20–60. The solid line represents the normal Gauss function.

events observed in coincidence with 156 GRBs during T_{90} for two N_{pad} ranges, respectively. For *Fermi* triggered GRBs, the position of the on-source window is set at the center of the error
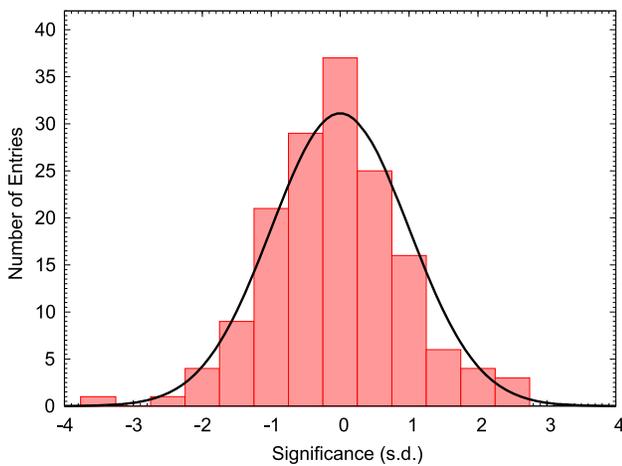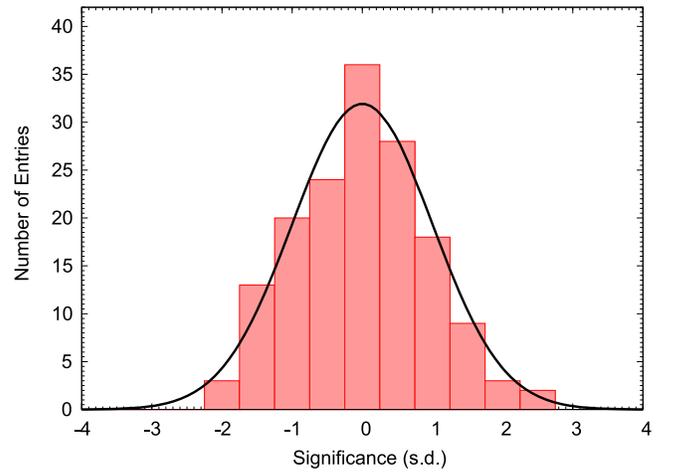

Figure 11. Significance distribution of the events detected in coincidence with the prompt phase of 156 GRBs, for the N_{pad} range of 20–500. The solid line represents a normal Gauss function.

box. No significance larger than three standard deviations is observed.

Given an excess with a number of detected events N_{on} during the interval T_{90} and an expected number of background events $\langle N_b \rangle$, we calculated the 99% confidence level (C. L.) upper limit on the number of signal events N_{UL}, by using the Feldman-Cousins prescription (Feldman & Cousins 1998). To determine the fluence corresponding to the number of events N_{UL}, we have to make assumptions regarding the spectral shape of the intrinsic GRB spectrum at high energy and take into account the absorption due to the EBL. According to the observations in the GeV range by CGRO-EGRET (Dingus 2001) and *Fermi*-LAT (Ackermann et al. 2013), the spectrum has usually a power-law shape and the value of the spectral index at high energy is around 2 ($\langle \alpha_{LAT} \rangle = 2.05 \pm 0.03$ for 35 GRBs see by *Fermi*-LAT). We assume an intrinsic power-law spectrum $dN/dE = KE^{-\alpha}$ with $\alpha = 2.0$, where the normalization K is obtained from the relation:

$$N_{UL} = K \int_{10\,\text{GeV}}^{E_{cut}} A_{eff} \cdot E^{-\alpha} \cdot e^{-\tau_{EBL}} \cdot dE, \qquad (2)$$

Here τ_{EBL} is the optical depth due to the EBL absorption, and E_{cut} is the maximum energy of the spectrum ($E_{cut} = 100\,\text{GeV}$ or 1 TeV). Concerning the EBL absorption, we use the Gilmore model with a semi-analytical approach (Gilmore et al. 2012), whose parameters at different energies and redshifts can be downloaded from the website.[26] Finally, the upper limit to the fluence F_{UL} is given by:

$$F_{UL} = K \int_{10\,\text{GeV}}^{E_{cut}} E \cdot E^{-\alpha} \cdot dE. \qquad (3)$$

Note that the redshift was measured for only 24 GRBs of our sample. For the bursts with unknown redshift, we calculate the EBL absorption assuming the mean observed redshift $z = 0.6$ for short GRBs ($T_{90} \leqslant 2$ s) and $z = 2.0$ for long GRBs ($T_{90} > 2$ s) (Berger et al. 2005; Jakobsson et al. 2006; Berger 2014).

Table 2 shows information on the 132 GRBs with unknown redshift, together with the calculated fluence upper limits that

---

[26] http://physics.ucsc.edu/~joel/EBLdata-Gilmore2012/

Table 2
List of 132 GRBs with Unknown Redshift That Occurred in the Field of View of ARGO-YBJ

GRB	Satellite	T_{90} (s)	θ(°)	keV fluence (10^{-7}erg cm^{-2}) (keV range)	σ_1 (10–100 GeV)	σ_2 (10–1000 GeV)	F_{UL1}(erg cm^{-2}) (10–100 GeV)	F_{UL2}(erg cm^{-2}) (10–1000 GeV)
(1)	(2)	(3)	(4)	(5)	(6)	(7)	(8)	(9)
080328	Swift	90.6	37.2	94 (15–150)	−0.04	−1.69	1.35E−2	4.56E−2
080515	Swift	21	43.2	20 (15–150)	−0.59	−0.41	7.77E−3	2.26E−2
080613B	Swift	105	39.2	58 (15–150)	0.89	1.32	2.57E−2	8.94E−2
080714086	Fermi	5.4	24.3	6.8 (10–1000)	1.82	0.71	1.14E−3	2.53E−3
080726	AGILE	12	36.7	⋯	1.50	1.03	7.20E−3	2.09E−2
080727C	Swift	79.7	34.5	52 (15–150)	−0.79	0.80	5.46E−3	3.29E−2
080730520	Fermi	17.4	31.2	48.7 (10–1000)	0.03	−0.20	2.31E−3	6.54E−3
080802386	Fermi	0.6	23.8	3.98 (10–1000)	−0.01	−0.70	7.57E−5	1.97E−5
080822B	Swift	64	40.4	1.7 (15–150)	−1.11	−2.00	1.57E−2	8.21E−2
080830368	Fermi	40.9	35.9	70 (10–1000)	0.41	1.36	7.99E−3	3.41E−2
080903	Swift	66	21.4	14 (15–150)	0.94	0.30	2.37E−3	5.94E−3
081025	Swift	23	30.6	19 (15–150)	0.84	0.69	3.33E−3	9.91E−3
081102365	Fermi	1.7	35.3	10.9 (10–1000)	−0.21	−1.01	4.77E−4	9.76E−5
081105	IPN	10	36.7	...	−0.90	−1.06	2.39E−3	1.22E−2
081122520	Fermi	23.3	9.9	75.4 (10–1000)	0.78	1.35	3.11E−3	2.79E−3
081130629	Fermi	45.6	37.9	32.2 (10–1000)	1.82	1.85	1.74E−2	5.80E−2
081215784	Fermi	5.6	31.3	547 (10–1000)	−0.56	0.09	1.02E−3	4.24E−3
081226156	Fermi	65.8	42.7	39.5 (10–1000)	−1.32	0.29	5.60E−3	4.97E−2
090107A	Swift	12.2	40.1	2.3 (15–150)	−0.99	−1.17	4.01E−3	2.84E−2
090118	Swift	16	13.4	4 (15–150)	−0.30	0.56	4.49E−4	2.09E−3
090301A	Swift	41	14.1	230 (15–150)	−1.25	−1.50	4.46E−4	1.13E−3
090301315	Fermi	23.3	22.8	22.7 (10–1000)	0.56	1.20	1.41E−3	5.30E−3
090306B	Swift	20.4	38.5	31 (15–150)	1.24	0.11	1.14E−2	2.51E−2
090320801	Fermi	29.2	22.4	16.7 (10–1000)	−0.33	0.20	1.02E−3	3.97E−3
090328713	Fermi	0.2	15.5	1.19 (10–1000)	−0.60	−0.27	2.10E−5	1.06E−5
090403314	Fermi	14.8	29.7	10.9 (10–1000)	−0.04	−0.64	1.74E−3	3.97E−3
090425377	Fermi	75.4	44.2	181 (10–1000)	−0.22	0.31	1.79E−2	5.41E−2
090511684	Fermi	7.6	39.0	24.9 (10–1000)	0.34	−1.18	5.74E−3	7.84E−3
090520A	Swift	20	42.2	3.4 (15–150)	1.27	0.67	1.54E−2	3.60E−2
090529564	Fermi	9.9	22.1	86.9 (10–1000)	−0.86	−0.42	4.36E−4	1.77E−3
090617208	Fermi	0.2	16.1	9.43 (10–1000)	−0.51	−0.77	2.27E−5	8.00E−6
090621B	Swift	0.14	40.5	0.7 (15–150)	0.20	0.40	4.84E−4	2.34E−4
090704783	Fermi	19.5	4.3	15.8 (10–1000)	0.13	−1.30	4.50E−4	6.41E−4
090712	Swift	145	10.6	40 (15–150)	0.93	0.47	1.96E−3	5.60E−3
090730608	Fermi	9.1	4.4	31.8 (10–1000)	0.82	−0.03	4.01E−4	1.01E−3
090802235	Fermi	0.1	35.5	11.4 (10–1000)	0.07	0.43	2.21E−4	9.37E−5
090807A	Swift	140.8	19.9	22 (15–150)	1.21	2.42	3.37E−3	1.39E−2
090807832	Fermi	17.9	29.3	13.4 (10–1000)	−0.07	−0.44	1.74E−3	4.56E−3
090820027	Fermi	12.4	17.0	1540 (10–1000)	0.80	1.09	7.37E−4	2.56E−3
090831317	Fermi	39.4	35.7	94.4 (10–1000)	−1.61	−2.11	1.96E−3	1.87E−3
090904A	Swift	122	22.0	30 (15–150)	0.16	0.45	2.57E−3	8.81E−3
090904581	Fermi	38.4	32.9	16.4 (10–1000)	−0.64	0.52	3.04E−3	1.64E−2
091030828	Fermi	98.1	25.0	296 (10–1000)	0.08	0.36	2.49E−3	8.84E−3
091106762	Fermi	14.6	30.2	18.3 (10–1000)	1.53	0.44	3.10E−3	6.86E−3
091202	Integral	45	33.2	⋯	−1.96	−0.72	7.40E−4	1.03E−2
091215234	Fermi	4.4	25.5	9.87 (10–1000)	−0.89	0.29	3.83E−4	2.20E−3
091227294	Fermi	21.9	27.9	68.9 (10–1000)	−0.86	−0.40	1.09E−3	4.40E−3
100111A	Swift	12.9	21.5	6.7 (15–150)	0.22	−0.28	8.06E−4	2.00E−3
100115A	Swift	3	32.6	⋯	−0.85	0.19	7.57E−4	4.30E−3
100122616	Fermi	22.5	33.1	120 (10–1000)	−0.25	0.01	2.96E−3	1.06E−2
100131730	Fermi	3.5	14.1	73.4 (10–1000)	0.29	1.43	2.91E−4	1.39E−3
100210101	Fermi	29.2	24.9	21.1 (10–1000)	0.89	1.44	2.04E−3	7.31E−3
100225703	Fermi	4.5	8.5	16.1 (10–1000)	0.76	0.11	3.07E−4	8.19E−4
100513879	Fermi	11.1	38.7	37.1 (10–1000)	−1.57	−0.71	1.74E−3	1.26E−2
100522A	Swift	35.3	27.7	21 (15–150)	−0.30	−1.15	1.79E−3	3.17E−3
100525744	Fermi	1.5	13.7	6.44 (10–1000)	0.74	0.68	7.83E−5	3.10E−5
100526A	Swift	102	9.6	25 (15–150)	−0.33	−0.07	9.87E−4	3.70E−3
100527795	Fermi	184.6	33.3	139 (10–1000)	−1.93	−1.89	1.00E−2	3.13E−2
100614498	Fermi	172.3	43.2	196 (10–1000)	−0.16	−0.80	3.96E−2	7.36E−2
100625891	Fermi	29.2	15.4	14 (10–1000)	−0.43	−0.88	6.60E−4	1.50E−3
100713A	Integral	20	12.6	210 (20–200)	−0.56	−0.30	4.09E−4	1.53E−3
100714686	Fermi	5.6	39.9	15.6 (10–1000)	0.08	−0.24	4.84E−3	1.32E−2

Table 2
(Continued)

| GRB	Satellite	T_{90} (s)	$\theta(°)$	keV fluence $(10^{-7}\text{erg cm}^{-2})$ (keV range)	σ_1 (10–100 GeV)	σ_2 (10–1000 GeV)	$F_{\text{UL1}}(\text{erg cm}^{-2})$ (10–100 GeV)	$F_{\text{UL2}}(\text{erg cm}^{-2})$ (10–1000 GeV)
(1)	(2)	(3)	(4)	(5)	(6)	(7)	(8)	(9)
100902A	Swift	428.8	37.1	32 (15–150)	1.08	0.75	3.99E–2	1.19E–1
101003244	Fermi	10	30.8	22.3 (10–1000)	1.71	0.51	2.91E–3	6.30E–3
101101744	Fermi	3.3	25.5	6.5 (10–1000)	0.07	−1.02	5.67E–4	9.41E–4
101107011	Fermi	375.8	25.8	72.6 (10–1000)	2.55	0.51	1.79E–2	3.59E–2
101112984	Fermi	82.9	39.8	85.7 (10–1000)	−0.71	−0.89	9.16E–3	2.56E–2
101123952	Fermi	103.9	28.2	1130 (10–1000)	1.49	0.99	6.39E–3	1.71E–2
101202154	Fermi	18.4	38.0	14.1 (10–1000)	−1.85	−1.58	1.26E–3	6.61E–3
101231067	Fermi	23.6	23.9	168 (10–1000)	0.32	−0.24	1.36E–3	3.24E–3
110106A	Swift	4.3	34.9	3 (15–150)	0.65	0.77	2.61E–3	9.01E–3
110210A	Swift	233	23.0	9.6 (15–150)	0.19	−0.16	3.87E–3	1.02E–2
110220761	Fermi	33	31.0	21.1 (10–1000)	−0.99	1.17	1.71E–3	1.41E–2
110226989	Fermi	14.1	36.9	19 (10–1000)	−1.16	−0.86	2.36E–3	9.74E–2
110312A	Swift	28.7	37.2	8.2 (15–150)	−0.002	0.84	6.91E–3	3.13E–2
110315A	Swift	77	19.4	41 (15–150)	0.26	0.96	1.73E–3	6.66E–3
110328520	Fermi	141.3	17.2	190 (10–1000)	−0.97	−0.96	1.27E–3	4.00E–3
110401920	Fermi	2.4	15.3	15.7 (10–1000)	−1.15	−1.00	1.13E–4	4.11E–4
110406A	Integral	8	31.1	⋯	0.85	0.35	2.13E–3	5.60E–2
110414A	Swift	152	44.2	35 (15–150)	−0.84	−0.69	1.93E–2	4.69E–2
110517573	Fermi	23	29.5	87.4 (10–1000)	−0.65	0.06	1.47E–2	6.50E–3
110605183	Fermi	82.7	33.8	193 (10–1000)	−1.30	−0.24	2.57E–3	1.80E–2
110625A	Swift	44.5	40.0	280 (15–150)	−1.07	−1.39	6.61E–3	1.53E–2
110626448	Fermi	6.4	40.4	11.6 (10–1000)	−0.003	−0.22	5.20E–3	1.47E–2
110629174	Fermi	61.7	5.1	24.3 (10–1000)	0.40	1.18	9.09E–4	3.96E–3
110705364	Fermi	19.2	18.7	89.4 (10–1000)	0.56	0.99	9.10E–4	3.30E–3
110706202	Fermi	12	26.9	32.7 (10–1000)	−0.22	−1.41	1.02E–3	1.34E–3
110706977	Fermi	33.2	29.3	65.5 (10–1000)	−1.41	−1.11	8.93E–4	3.82E–3
110709A	Swift	44.7	13.5	100 (15–150)	−0.35	−0.11	7.56E–4	2.73E–3
110709463	Fermi	24.1	26.7	69.1 (10–1000)	0.34	0.79	1.80E–3	6.47E–3
110820A	Swift	256	41.7	8.2 (15–150)	−0.07	0.16	3.31E–2	1.05E–1
110915A	Swift	78.76	39.5	57 (15–150)	0.42	−0.34	1.84E–2	4.20E–2
110919634	Fermi	35.07	42.6	268 (10–1000)	−0.63	−1.36	9.27E–3	1.43E–2
110921A	Swift	48	7.3	24 (15–150)	−0.30	−0.25	6.40E–4	2.21E–3
110928180	Fermi	148.2	8.5	142 (10–1000)	0.45	0.28	1.49E–3	4.69E–3
111017657	Fermi	11.1	40.0	207 (10–1000)	1.78	2.28	1.16E–2	4.17E–2
111024A	MAXI	0.2	10.7	⋯	−0.20	−0.30	2.06E–5	8.33E–6
111103B	Swift	167	41.6	80 (15–150)	0.23	−0.22	3.06E–2	4.04E–2
111109873	Fermi	9.7	32.1	66.9 (10–1000)	−0.26	0.81	1.66E–3	8.16E–3
111117A	Swift	0.47	38.5	1.4 (15–150)	2.18	1.80	1.12E–3	3.66E–4
111127810	Fermi	19	30.2	86.4 (10–1000)	0.81	−1.63	2.74E–3	1.83E–3
111208A	Swift	20	11.1	9.8 (15–150)	−1.54	−0.12	1.70E–4	1.59E–3
111215A	Swift	796	30.6	45 (15–150)	−3.51	−1.21	1.35E–2	2.04E–2
111228453	Fermi	2.9	23.9	27.5 (10–1000)	0.479	1.68	5.37E–4	2.44E–3
120102A	Swift	38.7	44.8	43 (15–150)	−1.80	−1.36	3.14E–3	1.34E–2
120106A	Swift	61.6	35.4	9.7 (15–150)	−0.27	0.26	6.76E–3	2.77E–2
120118898	Fermi	17.2	18.2	16.2 (10–1000)	−0.75	−1.26	4.53E–4	9.46E–4
120129A	IPN	4	38.5	⋯	−0.44	−0.01	2.71E–3	1.12E–2
120202A	Integral	100	15.6	0.7 (20–200)	−0.98	0.38	8.43E–4	5.17E–3
120217808	Fermi	5.9	38.8	17.5 (10–1000)	−0.74	1.01	2.77E–3	1.96E–2
120219A	Swift	90.5	32.1	5.4 (15–150)	−1.09	−1.25	3.16E–3	8.56E–3
120222021	Fermi	1.1	44.1	17.3 (10–1000)	2.39	1.72	1.74E–3	6.81E–4
120223933	Fermi	14.3	37.6	38.8 (10–1000)	0.46	0.003	6.28E–3	1.71E–2
120226447	Fermi	14.6	36.9	58.5 (10–1000)	−0.003	−1.51	4.83E–3	5.44E–3
120512A	Integral	40	36.8	⋯	−2.52	−0.34	6.90E–3	2.10E–2
120519721	IPN	0.96	43.8	24.1 (15–150)	0.06	−0.05	7.83E–4	3.48E–4
120522361	Fermi	28.2	40.2	93.2 (10–1000)	0.17	−0.59	1.10E–2	2.37E–2
120612680	Fermi	63.2	21.5	20.6 (10–1000)	−0.31	−0.70	1.47E–3	3.71E–3
120625119	Fermi	7.4	21.2	102 (10–1000)	−0.89	0.21	3.37E–4	1.87E–3
120703498	Fermi	77.6	21.8	26 (10–1000)	0.49	0.47	2.29E–3	6.97E–3
120819A	Swift	71	42.3	14 (15–150)	0.29	0.91	2.00E–2	6.87E–2
120905657	Fermi	195.6	41.9	195.7 (10–1000)	−0.30	−0.15	2.67E–2	8.16E–2
120915474	Fermi	5.9	40.9	3.8 (10–1000)	0.08	−0.57	5.47E–3	1.20E–2

Table 2
(Continued)

GRB	Satellite	T_{90} (s)	θ(°)	keV fluence (10^{-7}erg cm^{-2}) (keV range)	σ_1 (10–100 GeV)	σ_2 (10–1000 GeV)	F_{UL1}(erg cm^{-2}) (10–100 GeV)	F_{UL2}(erg cm^{-2}) (10–1000 GeV)
(1)	(2)	(3)	(4)	(5)	(6)	(7)	(8)	(9)
121011A	*Swift*	75.6	19.3	27 (15–150)	1.10	0.38	2.29E–3	5.66E–3
121012724	*Fermi*	0.45	24.5	12.7 (10–1000)	0.19	0.57	7.83E–5	3.26E–5
121025A	*MAXI*	20	6.9	⋯	−0.42	−0.72	3.61E–4	1.04E–3
121108A	*Swift*	89	36.2	9.6 (15–150)	0.19	−0.10	1.18E–2	3.24E–2
121113544	*Fermi*	95.5	34.5	268.5 (10–1000)	−0.32	−1.07	7.43E–3	1.39E–2
121123A	*Swift*	317	42.1	150 (15–150)	0.25	0.60	4.38E–2	1.38E–1
121202A	*Swift*	20.1	27.2	12 (15–150)	0.99	1.81	2.10E–3	8.04E–3
121211695	*Fermi*	9.0	23.7	13.4 (10–1000)	0.31	0.83	8.39E–4	3.11E–3
130122A	*Swift*	64	30.6	7.4 (15–150)	0.48	−0.53	4.85E–3	8.94E–3

Note. Column 1: GRB name (GCN name for *Swift* GRBs and Trigger ID for *Fermi* GRBs). Column 2: satellite that detected the GRB. Column 3: burst duration T_{90} as measured by the respective satellite. Column 4: zenith angle at the ARGO-YBJ location. Column 5: fluence in the keV range measured by the satellite that detected the burst. Columns 6 and 7: statistical significance of the events detected during the prompt phase, for two values of E_{cut} (100 GeV and 1 TeV). Columns 8 and 9: 99% C. L. upper limits to the fluence for two values of E_{cut} (100 GeV and 1 TeV).
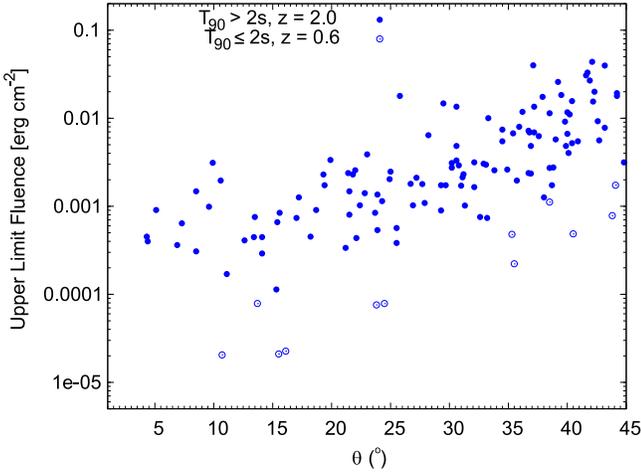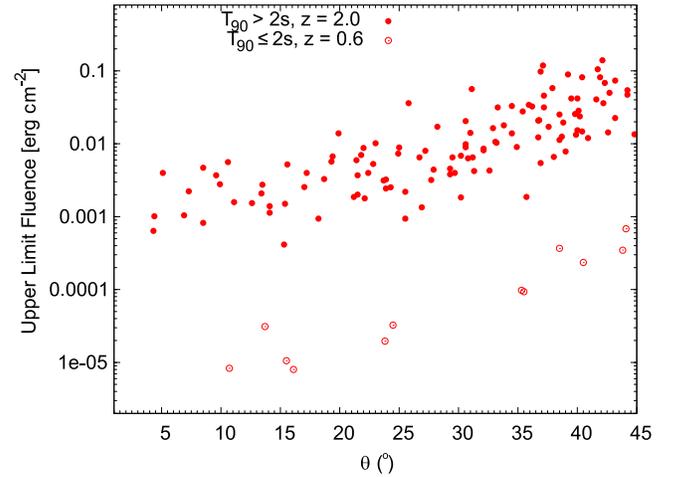

Figure 12. Fluence upper limits for $E_{cut} = 100$ GeV as a function of the zenith angle. Full dots are for long GRBs, circles for short ones.

Figure 13. Fluence upper limits for $E_{cut} = 1$ TeV as a function of the zenith angle. Full dots are for long GRBs, circles for short ones.

are in the range of $\sim 10^{-5}$–10^{-2} erg cm^{-2} for $E_{cut} = 100$ GeV and $\sim 10^{-5}$–10^{-1} erg cm^{-2} for $E_{cut} = 1$ TeV.

Figures 12 and 13 show the fluence upper limits as a function of the zenith angle for the two energy ranges considered, respectively. The upper limits increase with the zenith angle, due to the shower absorption at larger atmospheric thickness. In both figures, it is evident that short GRBs (assumed at $z = 0.6$) have upper limits much smaller than long GRBs (assumed at $z = 2.0$), due to the lower effect of the EBL absorption.

For the 24 GRBs with known redshifts, a more accurate estimation of the absorption can be done, providing more reliable fluence upper limits, given in Table 3 together with the GRB data. Also, in this case, the fluence limits are calculated assuming the spectral slope $\alpha = 2.0$. However, for GRB 090902B, the spectral slope $\alpha = 1.94$ measured by *Fermi*-LAT is used.

Figure 14 shows the F_{UL} values as a function of redshift, for the two energy ranges considered in the analysis. The fluence upper limits increase with redshift, since the flux is more absorbed for far sources. It is interesting to note that, for a given GRB, the fluence for $E_{cut} = 100$ GeV is higher than that

for $E_{cut} = 1$ TeV when $z < 1$; for $z > 1$, the situation is reversed, due to the large absorption of photons with energy above 100 GeV for $z > 1$.

Among the GRBs that occurred in the ARGO-YBJ field of view, GRB 090902B is the *Fermi*-GBM burst with the highest energy photon (33.4 GeV) detected by *Fermi*-LAT (Abdo et al. 2009), and for this reason it deserves special attention. The location was precisely determined by *Swift*, corresponding to a zenith angle of 23°.3 in the ARGO-YBJ field of view. The value of T_{90} is 19.3 s, the redshift is 1.82, and the spectral index is 1.94. According to our analysis, the cluster of events observed by ARGO-YBJ at the burst trigger time inside the interval T_{90} for the two N_{pad} ranges (20–60) and (20–500) have significances of −0.89 and −1.02 s.d., respectively. Since the 33.4 GeV photon was detected 82 s after the GBM trigger, i.e., about a minute after the end of the prompt emission, we did a search in coincidence with this delayed GeV emission. We considered three time windows: (a) the interval (0–90 s), including the most energetic photon, (b) the interval (6–26 s), when the maximum density of GeV photons has been observed, (c) the interval (82–83 s), i.e.,

Table 3
List of 24 GRBs with Known Redshifts That Occurred in the Field of View of ARGO-YBJ

GRB	Satellite	α_{SAT}	z_{SAT}	T_{90} (s)	θ (°)	keV fluence (10^{-7}erg cm^{-2}) (keV range)	σ_1 (10–100 GeV)	σ_2 (10–1000 GeV)	F_{UL1} (erg cm^{-2}) (10–100 GeV)	F_{UL2} (erg cm^{-2}) (10–1000 GeV)
(1)	(2)	(3)	(4)	(5)	(6)	(7)	(8)	(9)	(10)	(11)
071112C	Swift	1.09	0.82	15	18.42	30 (15–150)	0.25	0.12	8.90E−4	4.70E−4
080207	Swift	1.58	2.09	340	27.7	61 (15–150)	−0.24	0.15	7.29E−3	2.78E−2
080602	Swift	1.43	1.82	74	41.9	32 (15–150)	0.63	1.63	1.94E−2	6.48E−2
081028A	Swift	1.25	3.04	260	29.9	37 (15–150)	2.43	0.81	2.90E−2	1.14E−1
081128	Swift	1.98	<4	100	31.8	23 (15–150)	0.05	−0.80	1.64E−2	1.11E−1
090407	Swift	1.73	1.45	310	45	11 (15–150)	−0.78	0.16	1.58E−2	3.86E−2
090417B	Swift	1.85	0.35	260	37.2	23 (15–150)	−0.52	0.12	5.91E−3	9.93E−4
090424	Swift	1.19	0.54	48	33.1	210 (15–150)	−0.15	−0.06	1.56E−3	4.47E−4
090529A	Swift	2.00	2.63	100	19.9	6.8 (15–150)	−0.76	0.12	2.09E−3	1.53E−2
090902B	Fermi	1.94	1.82	19.3	23.3	4058 (10 keV– 10 GeV)	−0.89	−1.02	5.32E−4	1.34E−3
100206A	Swift	0.63	0.41	0.12	26.8	1.4 (15–150)	−0.71	0.85	3.80E−5	2.49E−5
100418A	Swift	2.16	0.62	7	18.7	3.4 (15–150)	−0.72	−0.59	1.07E−4	2.55E−5
100424A	Swift	1.83	2.47	104	33.4	15 (15–150)	1.43	1.70	1.71E−2	8.40E−2
100728A	Swift	1.18	1.57	198.5	44.9	380 (15–150)	0.55	0.19	2.51E−2	3.58E−2
101224A	Swift	1.05	0.72	0.2	22.6	0.58 (15–150)	−0.10	−0.42	4.70E−5	2.16E−5
110106B	Swift	1.76	0.62	24.8	25.1	20 (15–150)	−1.40	−0.83	1.80E−4	1.22E−4
110128A	Swift	1.31	2.34	30.7	43.2	7.2 (15–150)	−0.06	0.16	1.63E−2	5.66E−2
111211A	AGILE	2.77	0.48	15	20.3	92 (20-1200)	0.16	0.16	2.45E−4	6.41E−5
120118B	Swift	2.08	2.94	23.2	42.7	18 (15–150)	−0.71	−0.45	1.53E−2	7.77E−2
120326A	Swift	2.06	1.8	69.6	41.0	26 (15–150)	−0.24	0.25	1.22E−2	3.80E−2
120716A	IPN	CPL	2.49	230	35.7	147 (10–1000)	−1.39	−1.32	9.01E−3	4.61E−2
120722A	Swift	1.90	0.96	42.4	17.7	12 (15–150)	−0.18	−0.80	4.20E−4	2.36E−4
120907A	Swift	1.73	0.97	16.9	40.2	6.7 (15–150)	0.10	0.38	3.46E−3	3.34E−3
130131B	Swift	1.15	2.54	4.3	27.3	3.4 (15–150)	0.80	0.19	1.45E−3	5.91E−3

Note. Column 1: GRB name (GCN name for *Swift* GRBs and Trigger ID for *Fermi* GRBs). Column 2: satellite that detected the burst. Column 3: spectral index reported by the satellite: "CPL" means that the spectrum measured by the satellite is fitted with a cutoff power law. Others are fitted by a simple power law. Column 4: redshift. Column 5: burst duration T_{90} as measured by the respective satellite. Column 6: zenith angle at the ARGO-YBJ location. Column 7: fluence in the keV range measured by the satellite that detected the burst. Columns 8 and 9: statistical significance of the events detected during the prompt phase, for two E_{cut} values (100 GeV and 1 TeV). Columns 10 and 11: 99% C. L. upper limits to the fluence for two E_{cut} values (100 GeV and 1 TeV) with $\alpha = 2.0$ ($\alpha = 1.94$ for GRB 090902B).
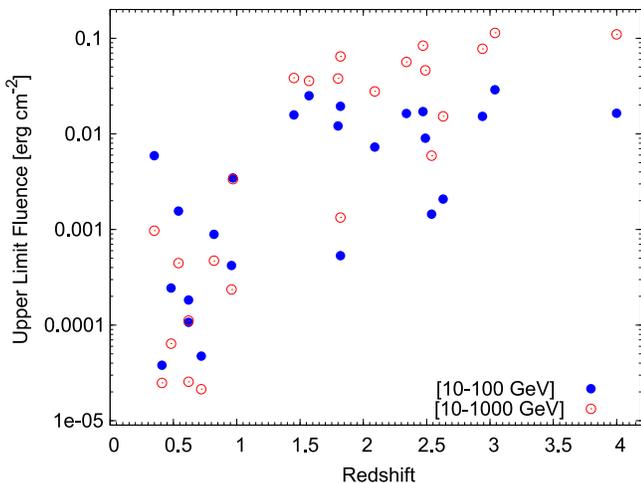
Figure 14. Fluence upper limits as a function of redshift.

the time around the 33.4 GeV photon. The significance of the events detected in the three time windows are −1.53, −1.05, and −0.07 s.d., respectively, for $N_{pad} = 20$–60, and −0.45, −0.41, and 0.74 s.d., respectively, for $N_{pad} = 20$–500. Using the set of time windows for the standard analysis, the maximum significance is 4.33 s.d. for a time interval of 3 s delayed 2047 s since the burst trigger time. After taking into account the

number of trials, the significance lowers to 0.22 s.d. leading to the conclusion that there are no significant excesses associated with this GRB. Following the method described at the beginning of this section, we evaluated the fluence upper limit in T_{90} at the prompt phase. We found $F_{UL} = 5.32 \times 10^{-4}$ erg cm^{-2} (1.74×10^{-4} erg cm^{-2} without correction for the EBL absorption) in the energy range of 10–100 GeV to be compared with the extrapolated fluence $F_{EX} = 1.06 \times 10^{-4}$ erg cm^{-2} (obtained by extrapolating up to E_{cut} the flux measured by satellite, taking into account the EBL attenuation). In the energy range of 10–1000 GeV, we found $F_{UL} = 1.34 \times 10^{-3}$ erg cm^{-2} (4.63×10^{-6} erg cm^{-2} without correction for EBL absorption) to be compared with $F_{EX} = 2.28 \times 10^{-4}$ erg cm^{-2}. Taking into account the EBL absorption, the extrapolated fluences of GRB 090902B are lower than the upper limits measured by ARGO-YBJ. According to our calculations, ARGO-YBJ could detect GRB 090902B for a redshift less than 1.0 and an emission extending up to 1 TeV.

6. Detectability of GRB 130427A

GRB 130427A, detected by both *Fermi*-GBM and *Fermi*-LAT, is the burst with the highest energy photons ever observed, reaching 95 GeV. ARGO-YBJ was switched off in 2013 February, two months before the burst, but since the zenith angle of the GRB was greater than 90°, the burst would have

been undetectable in any case. It is interesting, however, to estimate the capability of ARGO-YBJ to detect a burst as bright as GRB 130427A, in case of a more favorable zenith angle.

The measured spectral index of GRB 130427A ranges between $\alpha \sim 2.5$ and $\alpha \sim 1.7$, the total fluence in the 10 keV–100 GeV band is 4.9×10^{-3} erg cm^{-2} and the duration is $T_{90} = 138.2$ s (Ackermann et al. 2014). Assuming a zenith angle $\theta = 20°$, a spectral index $\alpha = 2.0$, and considering the EBL absorption corresponding to the GRB distance ($z = 0.34$), the estimated minimum fluence detectable by ARGO-YBJ in T_{90} is 1.27×10^{-3} erg cm^{-2} in the energy range of 10–100 GeV, and 2.38×10^{-4} erg cm^{-2} in the energy range of 10–1000 GeV. Assuming a spectrum extending up to 1 TeV with the same spectral index, the fluence of GRB 130427A in the energy range of 10–1000 GeV would be 4.7×10^{-4} erg cm^{-2}, twice higher than the ARGO-YBJ sensitivity. Thus, an overhead burst as bright as GRB 130427A and with a photon emission extending up to 1 TeV would have been easily detected by ARGO-YBJ.

7. Conclusions

A search for GeV–TeV burst-like events in coincidence with GRBs detected by satellite was done using the ARGO-YBJ data from 2007 November 6 to 2013 February 7. During more than five years, a total of 156 GRBs was analyzed. After considering the number of trials, the distribution of the chance probabilities of the events occurred in coincidence with the GRBs (i.e., during T_{90}) or in the sliding time windows inside the interval of one hour after the satellite trigger time is consistent with background fluctuations. None of the examined GRBs, notably the "*Swift* GRBs", contains high energy (>10 GeV) photons with fluxes comparable to that featuring GRB 130427A and spectrum extending up to 1 TeV. Indeed, many conditions, such as the efficiency of the production mechanism, the source transparency, and the attenuation by the EBL, may affect the GeV–TeV fluence.

Since no significant signal has been detected, the 99% C. L. upper limits to the energy fluence were evaluated. The limits are calculated assuming a power-law energy spectrum with spectral index $\alpha = 2.0$ above 10 GeV, a sharp cutoff at the $E_{\rm cut}$ energy (100 GeV or 1 TeV), and taking into account the EBL absorption (assuming a redshift $z = 0.6$ for short GRBs and $z = 2.0$ for long GRBs when the redshift was not available). The obtained fluence upper limits cover a large range of values, depending on the GRB duration, zenith angle, and distance, ranging from less than 10^{-5} erg cm^{-2} to 10^{-1} erg cm^{-2}.

In the next future, HAWC, CTA and LHAASO (these two currently under construction), given their significantly higher sensitivity, are expected to provide the first measurement of the GeV–TeV emission from gamma-ray bursts by ground-based detectors.

References

Aartsen, M. G., Abraham, K., Ackermann, M., et al. 2016, ApJ, 824, 115
Abdo, A. A., Ackermann, M., Ajello, M., et al. 2009, ApJL, 706, L138
Abdo, A. A., Allen, B. T., Berley, D., et al. 2007, ApJ, 666, 361
Abeysekara, A. U., Alfaro, R., Alvarez, C., et al. 2015, ApJ, 800, 78
Abramowski, A., Aharonian, F., Ait Benkhali, F., et al. 2014, A&A, 565, A16
Acciari, V. A., Aliu, E., Arlen, T., et al. 2011, ApJ, 743, 62
Ackermann, M., Ajello, M., & Asano, K. 2013, ApJS, 209, 11
Ackermann, M., Ajello, M., Asano, K., et al. 2014, Sci, 343, 42
Aglietta, M., Alessandro, B., Antonioli, P., et al. 1996, ApJ, 469, 305
Agostinelli, S., Allison, J., Amako, K., et al. 2003, NIMPA, 506, 250
Aielli, G., Assiro, R., Bacci, C., et al. 2006, NIMPA, 562, 92
Aielli, G., Bacci, C., Barone, F., et al. 2009a, ApJ, 699, 1281
Aielli, G., Bacci, C., Bartoli, B., et al. 2009b, APh, 32, 47
Albert, J., Aliu, E., Anderhub, H., et al. 2006, ApJL, 641, L9
Aleksić, J., Ansoldi, S., Antonelli, L. A., et al. 2014, MNRAS, 437, 3103
Amenomori, M., Cao, Z., Dai, B. Z., et al. 1996, A&A, 311, 919
Atkins, R., Benbow, W., Berley, D., et al. 2000, ApJL, 533, L119
Atkins, R., Benbow, W., Berley, D., et al. 2005, ApJ, 630, 996
Bartoli, B., Bernardini, P., Bi, X. J., et al. 2013, ApJ, 779, 27
Bartoli, B., Bernardini, P., Bi, X. J., et al. 2014a, ApJ, 794, 82
Bartoli, B., Bernardini, P., Bi, X. J., et al. 2014b, ApJ, 790, 152
Bartoli, B., Bernardini, P., Bi, X. J., et al. 2015a, ApJ, 806, 20
Bartoli, B., Bernardini, P., Bi, X. J., et al. 2015b, PhRvD, 92, 092005
Bartoli, B., Bernardini, P., Bi, X. J., et al. 2015c, PhRvD, 91, 112017
Beloborodov, A. M., Hascoët, R., & Vurm, I. 2014, APJ, 788, 36
Berger, E. 2014, ARA&A, 52, 43
Berger, E., Kulkarni, S. R., Fox, D. B., et al. 2005, ApJ, 634, 501
Berger, E., Kulkarni, S. R., Pooley, G., et al. 2003, Natur, 426, 154
Bloom, J. S., Prochaska, J. X., Pooley, D., et al. 2006, ApJ, 638, 354
Campana, S., Mangano, V., Blustin, A. J., et al. 2006, Natur, 442, 1008
Castellina, A., Ghia, P. L., Kakimoto, F., et al. 2001, NCimC, 24, 631
Chen, S. Z., Di Girolamo, T., He, H. H., et al. 2015, Proc. 34th ICRC (the Hague, the Netherlands), PoS (ICRC2015), 728
Connaughton, V., Briggs, M. S., Goldstein, A., et al. 2015, ApJS, 216, 32
Cusumano, G., Mangano, V., Angelini, L., et al. 2006, ApJ, 639, 316
Dermer, C. D., & Chiang, J. 2000, in AIP Conf. Proc. 515, GeV to TeV Gamma-Ray Astrophysics Workshop: towards a major atmospheric Cherenkov detector VI, ed. B. L. Dingus (Melville, NY: AIP), 225
Ding, L. K., Zhaxi, C. R., Zhaxi, S. Z., et al. 1997, HEPNP, 21, 673
Dingus, B. L. 2001, in AIP Conf. Proc. 558, High Energy Gamma-Ray Astronomy: International Symposium, ed. F. A. Aharonian & H. J. Voelk (Melville, NY: AIP), 383
Feldman, G. J., & Cousins, R. D. 1998, PhRvD, 57, 3873
Fox, D. B., Frail, D. A., Price, P. A., et al. 2005, Natur, 437, 845
Gilmore, R. C., Somerville, R. S., Primack, J. R., et al. 2012, MNRAS, 422, 3189
Hascoët, R., Vurm, I., & Beloborodov, A. M. 2015, ApJ, 813, 63
Hurley, K., Dingus, B. L., Mukherjee, R., et al. 1994, Natur, 372, 652
Inoue, S., Granot, J., O'BrienInoue, P. T., et al. 2013, APh, 43, 252
Jakobsson, P., Levan, A., Fynbo, J. P. U., et al. 2006, A&A, 447, 897
Klebesadel, R. W., Strong, I. B., & Olson, R. A. 1973, ApJL, 182, L85
Kouveliotou, C., Meegan, C. A., Fishman, G. J., et al. 1993, ApJL, 413, L101
Larsson, J., Racusin, J. L., & Burgess, J. M. 2015, ApJL, 800, L34
Ma, X. H., Zhou, X. X., Wu, M., et al. 2003, HEPNP, 27, 973
Meegan, C. A., Fishman, G. J., Wilson, R. B., et al. 1992, Natur, 355, 143
Metzger, M. R., Djorgovski, S. G., Kulkarni, S. R., et al. 1997, Natur, 387, 878
Narayana Bhat, P., Meegan, C. A., Von Kienlin, A., et al. 2016, ApJS, 223, 28
Padilla, L., Funk, B., Krawczynski, H., et al. 1998, A&A, 337, 43
Pe'er, A., & Waxman, E. 2004, ApJ, 613, 448
Poirier, J., D'Andrea, C., Fragile, P. C., et al. 2003, PhRvD, 67, 042001
Rosswog, S., Ramirez-Ruiz, E., & Davies, M. B. 2003, MNRAS, 345, 1077
Salvaterra, R., Valle, M. D., Campana, S., et al. 2009, Natur, 461, 1258
Van, P. J., Groot, P. J., Galama, T., et al. 1997, Natur, 386, 686
Vernetto, S. 2000, APh, 13, 75
Zhang, B., Lü, H. J., & Liang, E. W. 2016, SSRv, 202, 3
Zhou, X. X. & for the Tibet ASγ collaboration 2003, Proc. 28th ICRC, (Tsukuba, Japan), 2757
Zhou, X. X., Cheng, N., Hu, H. B., et al. 2007, HEPNP, 31, 65
Zhou, X. X., Gao, L. L., Zhang, Y., et al. 2016, ChPhC, 40, 075001
Zhou, X. X., Hu, H. B., & Huang, Q. 2009, AcPSn, 58, 5879